Journal of Materials Chemistry C

ROYAL SOCIETY OF CHEMISTRY

PAPER

View Article Online
View Journal | View Issue

Cite this: J. Mater. Chem. C, 2023, 11, 10684

Achieving excellent thermostable red emission in singly Mn^{2+}-doped near-zero thermal expansion (NZTE) material $Li_2Zn_3(P_2O_7)_2$†

Qin Liu,[abc] Peipei Dang,*[a] Guodong Zhang,[ab] Maxim S. Molokeev,[de] Sergey P. Polyutov,[d] Hongzhou Lian,[a] Ziyong Cheng,[a] Guogang Li*[cf] and Jun Lin*[ab]

Received 15th May 2023,
Accepted 4th July 2023

DOI: 10.1039/d3tc01683h

rsc.li/materials-c

The design of thermostable phosphor is still a pivotal challenge in pc-WLED applications. Herein, an efficient strategy is proposed to design excellent thermostable red emission in the singly Mn^{2+}-doped near-zero thermal expansion (NZTE) material $Li_2Zn_3(P_2O_7)_2$. Under the excitation of 412 nm wavelength, the emission could be tuned from 636 to 672 nm by increasing the Mn^{2+}-doping level *via* synthetic effects among the crystal field, the exchange coupling interaction in Mn–Mn dimers, and energy transfer in different luminescence centers. The PL intensity of LZPO:Mn^{2+} could be maintained at 97% at 150 °C and 94% at 200 °C of its initial intensity at room temperature. During the heating process, LZPO presented near-zero thermal expansion, contributing to the nearly unaffected PL intensity. The emission loss was also compensated by trap-assisted energy transfer to the luminescent center. This study not only offers a perspective idea for elucidating the correlation between the crystal structure and optical properties, but also opens a new way of designing excellent thermostable luminescent materials based on NZTE materials in self-reduction systems.

1. Introduction

With regard to the exceptional advantages of high color rendering, long service lifetime, low energy consumption, eco-friendliness, fast response, phosphor-converted white-light-emitting diodes (pc-WLEDs) play an important role in many areas, such as solid-state lighting, backlight displays, and information security.[1–6] Phosphors are one of the indispensable components in pc-WLED devices, and their photoluminescence (PL) thermal stability plays a crucial role in practical applications, which is usually evaluated by the thermal quenching (TQ) behavior.[7–10] Thermal quenching (TQ) is caused by the anabatic non-radiative relaxation of electrons from the excited state to the ground state at high working temperature.[11–14] It shortens the service lifetime of pc-WLED devices and restrains the widespread use of phosphors. Hence, it is necessary to explore luminescent materials with excellent thermal stability. However, the design of novel phosphors with excellent thermal stability is still a significant challenge. To date, much effort has been devoted to designing different strategies to solve the emission loss with increasing temperature. For example, defect engineering is a normal approach to achieve excellent PL thermal stability, such as in blue-emitting phosphors $Na_3Sc_2(PO_4)_3$:Eu^{2+},[1] yellow-emitting phosphors $LiZnPO_4$:xMn^{2+},[15] orange-red phosphors β-$KMg(PO_3)_3$:Mn^{2+},[16] and red-emitting phosphors $BaXP_2O_7$:Mn^{2+}(X = Mg/Zn),[17] $NaZn(PO_3)_3$:Mn^{2+}.[18] However, the precise control of defect position in the matrix lattice is still a challenge. Otherwise, energy transfer between the traps (or sensitizers) and the luminescence centers (activators) helps to gain excellent thermostable emission, such as in $SrGa_2Si_2O_8$:Mn^{2+},[19] $BaMgP_2O_7$: Eu^{2+}, Mn^{2+},[20] $Mg_3Y_2Ge_3O_{12}$:Eu^{3+}, Mn^{4+},[21] and $Ca_2LuZr_2Al_3O_{12}$:Cr^{3+},Yb^{3+}.[22] The efficiency of energy transfer is ultimately determined by the

[a] State Key Laboratory of Rare Earth Resource Utilization, Changchun Institute of Applied Chemistry, Chinese Academy of Science, Changchun 130022, P. R. China. E-mail: ppdang@ciac.ac.cn, jlin@ciac.ac.cn
[b] School of Applied Chemistry and Engineering, University of Science and Technology of China, Hefei 230026, P. R. China
[c] Faculty of Materials Science and Chemistry, China University of Geoscience, Wuhan 430074, P. R. China. E-mail: ggli@cug.edu.cn
[d] International Research Center of Spectroscopy and Quantum Chemistry—IRC SQC, Siberian Federal University, Krasnoyarsk, 660041, Russia
[e] Laboratory of Crystal Physics, Kirensky Institute of Physics, Federal Research Center KSC SB RAS, Krasnoyarsk, 660036, Russia
[f] Zhejiang Institute, China University of Geosciences, Hangzhou, 311305, P. R. China

† Electronic supplementary information (ESI) available: Refined structure parameters, emission peak position fitted by Gaussian method and corresponding lifetime of LZPO:xMn^{2+} samples. Rietveld refinement XRD pattern, the diffuse reflectance spectra of LZPO:xMn^{2+} (x = 0.05, 0.1, 0.3) phosphors. PL spectra and XPS spectrum of LZPO:0.1Mn^{2+}. Temperature-dependent PL spectra of LZPO:0.01Mn^{2+} with different Mn-source sintered in air and N_2(90%)-H_2(10%) atmosphere. See DOI: https://doi.org/10.1039/d3tc01683h

crystal structure, whereby the matrix should have suitable sites for both sensitizers and activators. Structural modulation can also be effective for enhancing PL thermal stability, such as in $(Zn,Mg)B_2O_4:Mn^{2+}$,[23] $(Sr,Ca)AlSiN_3:Eu^{2+}$,[24] and $Ca(Sc,Mg)(Al,Si)O_6:Cr^{3+}$.[25] Nevertheless, the luminescence properties of luminescent ions are influenced by the radius size, charge, and electronegativity of the matrix cations. In addition, choosing an ideal host with specific performance is an efficient way to achieve high PL thermal stability for luminescent ions. Many cases have been successfully reported, such as the zero thermal expansion (ZTE) material $Zn_4B_6O_{13}:Mn^{2+}$ phosphor,[26] negative thermal expansion (NTE) materials $Sc_2W_3O_{12}:Eu^{3+}$,[27] $Cs_3GdGe_3O_9:Eu^{3+}$,[28] and $Sc_2(MoO_4)_3:Yb^{3+}/Er^{3+}$,[29] and layered structural design of $MgIn_2P_4O_{14}:Tm^{3+},Dy^{3+}$,[30] and $SrIn_2P_4O_{14}:Tm^{3+},Dy^{3+}$, and so on.[31]

In this study, we synthesized a sequence of red-emitting $Li_2Zn_{3-x}(P_2O_7)_2:xMn^{2+}$ phosphors (abbreviated as LZPO:xMn^{2+}) by a high-temperature solid-state reaction method at ambient atmosphere. The compound $Li_2Zn_3(P_2O_7)_2$ was chosen as an ideal matrix material because of its outstanding structural stability. The rigid anionic groups $[P_2O_7]^{4-}$ were constructed to protect the Mn^{2+} ions from being oxidized at high temperature, which lay the foundation for the little TQ. At 150 °C, the PL intensity of the LZPO:Mn^{2+} red phosphor was 97% of that at room temperature, and even at 200 °C, the PL intensity of the LZPO:Mn^{2+} red phosphor was still 94%, demonstrating its excellent PL thermal stability. The corresponding kinetic mechanisms are discussed in detail *via* experimental analysis. Based on the Rietveld refinement method, the crystal structure was elucidated. The emission could be tuned from 636 to 672 nm by increasing the Mn^{2+}-doping level, and the corresponding luminescence mechanism was explored. These results indicate that the LZPO:Mn^{2+} phosphor could be a promising material in applications of high-power (HP) pc-WLEDs. This paper not only offers a perspective idea to reveal the correlation between the crystal structure and optical properties, but also initiates a new avenue of research for designing excellent thermostable luminescent materials based on NZTE materials.

2. Experimental

2.1. Materials and preparation

The as-prepared LZPO:xMn^{2+} (x = 0–0.5) phosphors were synthesized by a conventional high-temperature solid-state method under an air atmosphere. Li_2CO_3 (97%, A.R.), ZnO (≥99.0%, BEIJING SHIJI), MnO_2 (≥99.9%, Alfa Aesar), $MnCO_3$ (≥99.9%, Alfa Aesar), and $NH_4H_2PO_4$ (≥99.0%, BEIJING SHIJI) were used as the initial chemicals without further purification according to the stoichiometric ratios. The weighed mixtures were transferred to an agate mortar and ground thoroughly for 30 min. The samples were then put into an alumina crucible and sintered at 700 °C for 10 h, and cooled to room temperature. By an additional grinding, a fine powder was obtained for further characterization. Additionally, a series of LZPO:0.01Mn^{2+} phosphors samples with different Mn sources ($MnCO_3$, MnO_2) were synthesized under an air atmosphere and under a reduced atmosphere of N_2 (90%)–H_2 (10%) in the same way.

2.2. Characterizations

The phase purity was identified using X-ray diffraction (XRD) on a Bruker D8 ADVANCE powder diffractometer with Cu K_α radiation (λ = 1.54 Å) under 40 kV and 40 mA at room temperature. The scanning rate was 0.6° min^{-1}. XRD Rietveld profile refinements of the structural models were performed by using TOPAS 4.2. Diffuse reflectance (DR) measurements were recorded on the UV-visible-diffuse reflectance spectroscopy system UV-3600i Plus (Shimadzu Corporation, Japan). X-Ray photoelectron spectroscopy (XPS) was performed using an XPS microprobe system (Thermo SCIENTIFIC ESCALAB 250Xi). Electron paramagnetic resonance (EPR) spectra of the samples were obtained on a Bruker A300 spectrometer with the X-band (9.84 GHz) at room temperature. Thermoluminescence (TL) glow curves were measured using a TL spectroscopy system (TOSL-3DS) at a heating rate of 0.2 K s^{-1}. Photoluminescence excitation (PLE) and photoluminescence emission (PL) spectra were obtained on an Edinburgh Instruments FLSP-920 fluorescence spectrophotometer equipped with a 150 W xenon lamp as the excitation source. The temperature-dependent PL spectra were evaluated with the same instrument with a temperature controller. The room temperature PL lifetime decay curves of the as-prepared samples were recorded on the same spectrometer with 412 nm wavelength laser radiation as the excitation source. Photoluminescence quantum yield (PLQY) values were collected on an absolute PL quantum yield measurement system (C11347-11, Japan). The LED devices were fabricated by mixing commercial $BaMgAl_{11}O_{17}:Eu^{2+}$ (BAM:Eu^{2+}) blue phosphor, $(Ba,Sr)_2SiO_4:Eu^{2+}$ green phosphor, the as-prepared LZPO:0.1Mn^{2+} phosphor, and a commercial 365 nm UV chip. Luminescence measurements of the as-fabricated pc-WLED devices were carried out at 3.16 V voltage and at a 20–300 mA driving current. The electroluminescence (EL) performance of the pc-WLED devices were measured on a HAAS 2000 photoelectric measuring system (380–1100 nm, EVERFINE, China) with an integrating sphere.

3. Results and discussion

3.1. Phase identification and crystal structure analysis

Fig. 1a shows the crystal structure of $Li_2Zn_3(P_2O_7)_2$, which belongs to an orthorhombic phase with the space group *Pbcm* (57).[32] In this structure, there are two symmetry-independent sites for Zn atoms. Each Zn atom coordinates with five O atoms to form $[ZnO_5]$ trigonal bipyramids. The Zn1 site is completely occupied, while the Zn2 site is occupied by Zn^{2+} and Li^+ cations, and the Zn^{2+}/Li^+ ratio is 1 : 1. Half of the Li^+ cations are disordered at the partially occupied Zn2 positions. The other half are coordinated with four O atoms and at the interstitial positions. The two completely occupied $[Zn1O_5]$ and the partially occupied $[Zn2O_5]$ trigonal bipyramids are connected by a common edge to form $[Zn_2O_8]$ dimere. These $[Zn_2O_8]$ dimers alternately share edges to form $[ZnO_5]$ chains running along the c axis. The three-dimensional framework structure of $Li_2Zn_3(P_2O_7)_2$ is formed by $[ZnO_5]$ chains sharing tetrahedra vertices with $[P_2O_7]$ dimers. In order to analyze the phase

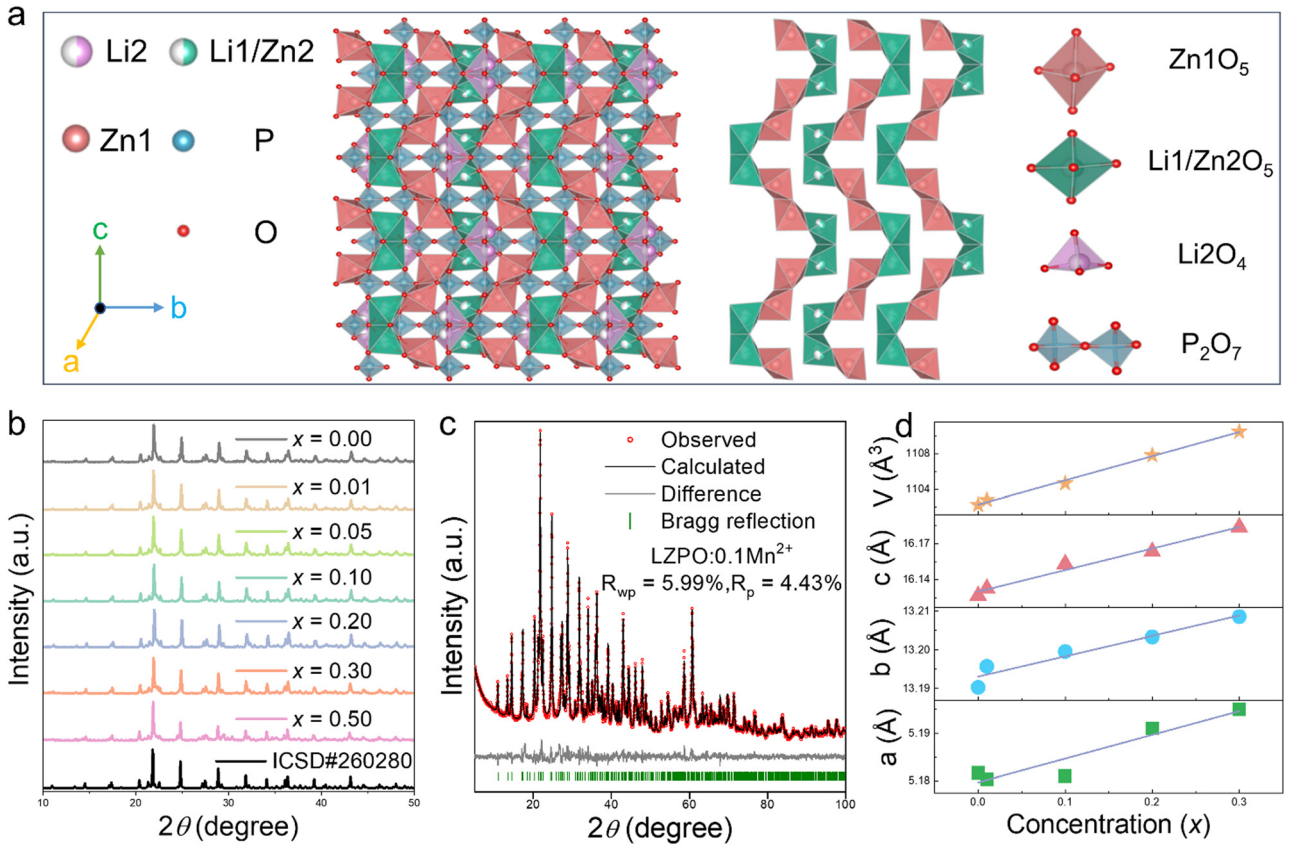

Fig. 1 (a) Crystal structure diagram of the LZPO host. (b) XRD patterns at 2θ = 10°–50° of $Li_2Zn_{3-x}(P_2O_7)_2$:xMn^{2+} (x = 0–0.5) samples. (c) Rietveld refinement of the LZPO:0.1Mn^{2+} sample. (d) Variation of the cell parameters (a)–(c) and cell volume (V) with the increase in Mn^{2+} concentration, respectively.

structure, the X-ray diffraction (XRD) patterns of LZPO:xMn^{2+} (x = 0, 0.01, 0.05, 0.1, 0.2, 0.3, 0.5) phosphors and the standard card (ICSD#260280) of $Li_2Zn_3(P_2O_7)$ were compared and are shown in Fig. 1b. The as-prepared LZPO:xMn^{2+} phosphors could be well indexed as pure phases according to the standard card, indicating that the incorporation of Mn^{2+} into the LZPO lattice had no effect on the phase purity. For getting more detailed information, Rietveld refinements of the LZPO:xMn^{2+} (x = 0, 0.01, 0.1, 0.2, 0.3) samples were performed (Fig. 1c and Fig S1a–d, ESI†). Tables S1–S3 (ESI†) list the refined structural parameters and cell parameter values. The LZPO host yielded a = 5.18166 (14) Å, b = 13.1903 (3) Å, c = 16.1267 (4) Å, $\alpha = \gamma = \beta = 90°$, V = 1102.22 (5) Å^3, and R_p = 4.08%, R_{wp} = 5.34%, χ^2 = 2.5. As for the LZPO:0.1Mn^{2+} sample, a = 5.18097 (18) Å, b = 13.1996 (4) Å, c = 16.1532 (5) Å, $\alpha = \gamma = \beta = 90°$, V = 1104.66 (6) Å^3, and R_p = 4.43%, R_{wp} = 5.99%, χ^2 = 2.51. Owing to having the same valence and a similar ionic radius, the Mn^{2+} (r = 0.75 Å, CN = 5) ions prefer to occupy the 5-coordination Zn^{2+} (r = 0.68 Å, CN = 5) sites in the lattice. As shown in Fig. 1d, the cell parameters and lattice volume showed a good linear increase *versus* the doping level x, which was caused by the replacement of the larger Mn^{2+} ions for Zn^{2+} ions. These results imply the synthesis of single Mn^{2+}-doped single-phase LZPO:xMn^{2+} materials and the successful integration of Mn^{2+} ions into the lattice.

3.2. Optical properties of LZPO:xMn^{2+} (x = 0.01–0.5) phophors

Fig. 2a displays the diffuse reflectance spectra of the LZPO host and LZPO:0.1Mn^{2+}, and photoluminescence excitation (PLE) spectrum of LZPO:0.1Mn^{2+}, respectively. The energy absorption of less than 230 nm came from the ultraviolet (UV) absorption of the matrix.

As for LZPO:0.1Mn^{2+}, the absorption of 270 nm was derived from the charge-transfer band of O^{2-}–Mn^{2+}. Another absorption band ranging from 400 to 450 nm was noted, originating from the d–d transition of Mn^{2+}.[33,34] In addition, there was a weak valley in the wavelength of about 600 nm in the diffuse reflection spectra of the LZPO:xMn^{2+} (x = 0.05, 0.1, 0.3) phosphors (Fig. S2, ESI†). All the samples showed the same valley due to the small number of high valence states of Mn, which was caused by the limited self-reduction ability of Mn^{2+} in the air condition. According to the literature research, this weak valley is similar to the absorption of $^4A_2 \rightarrow {}^4T_2$ for Mn^{4+},[35,36] and the absorption of $^3A_2 \rightarrow {}^3T_1$ (^3F) for Mn^{5+}.[37–39] The optical band gap of the undoped LZPO sample can be calculated by utilizing the Kubelka–Munk equations (see the inset of Fig. 2a):[40,41]

$$F(R)hv = C\left(hv - E_g\right)^{\frac{n}{2}} \quad (1)$$

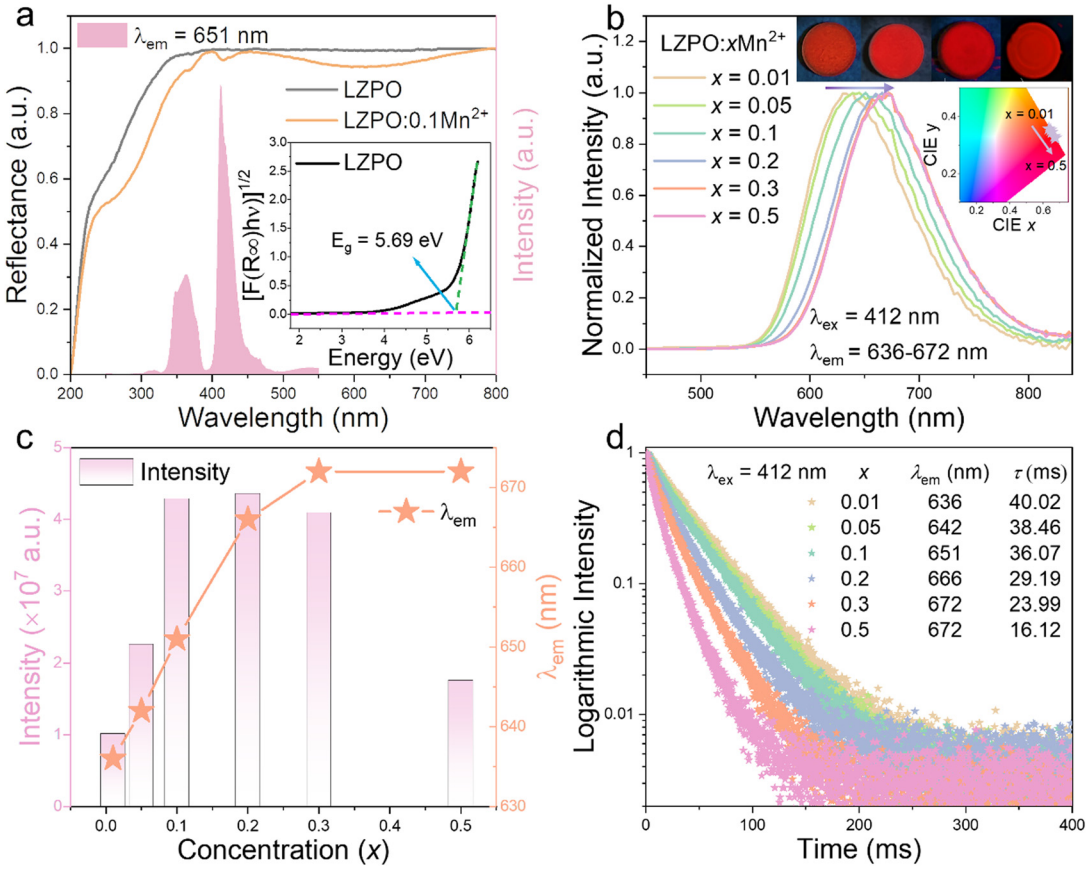

Fig. 2 (a) Diffuse reflectance spectra of LZPO and LZPO:0.1Mn^{2+} phosphors, PLE spectrum of LZPO:0.1Mn^{2+} (λ_{em} = 651 nm); inset plot shows $[F(R\infty)h\nu]^{1/2}$ *versus* $h\nu$ (eV). (b) Normalized PL spectra of LZPO:*x*Mn^{2+} (*x* = 0–0.5); inset shows the luminescent photographs of LZPO:*x*Mn^{2+} (*x* = 0.01, 0.1, 0.2, 0.3) phosphors under 365 nm wavelength excitation, and CIE color coordinates diagram of LZPO:*x*Mn^{2+} (*x* = 0.01–0.5) under 412 nm wavelength excitation. (c) Variations in the PL intensity and peak position as a function of the Mn^{2+}-doping concentration (*x*). (d) PL decay curves of LZPO:*x*Mn^{2+} (*x* = 0–0.5) monitored from 636 to 672 nm under 412 nm wavelength excitation.

$$F(R) = (1 - R^2)/2R \quad (2)$$

$$h\nu = \frac{1240}{\lambda} \quad (3)$$

where *R* represents the experimentally obtained reflectance, *h* is Planck's constant, *v* is the light frequency, *C* is a constant, E_g means the optical band gap, and λ is the absorption wavelength. Here, *n* is equal to 1 or 4 depending on whether the semiconductor is a direct or indirect type. Here, the value of *n* was 4. The calculated E_g value for LZPO was 5.69 eV, implying the LZPO host is an ideal matrix. According to the previous findings, a wide-bandgap host material is required to obtain temperature-stable Mn^{2+} luminescence in high-power pc-WLEDs.[42] By monitoring the emission peak at 651 nm for *x* = 0.1, the PLE spectrum covered the UV-vis region from 250 to 500 nm. The excitation band centered at 317 nm origined from the charge-transfer band (CTB) of Mn^{2+}–O^{2-}. Other bands centered at 347, 365, 412, and 467 nm were noted and ascribed to the spin-forbidden d–d transitions of Mn^{2+} from the ground state $^6A_1(^6S)$ to the excited states, $^4E(^4D)$, $^4T_2(^4D)$, $[^4A_1(^4G),^4E(^4G)]$, and $^4T_1(^4G)$, respectively.[43,44] Fig. S3 (ESI†) shows the typical photoluminescence (PL) emission spectra of the LZPO:*x*Mn^{2+} (*x* = 0.01–0.5) samples. Upon excitation at 412 nm wavelength, the asymmetric PL spectrum of LZPO:*x*Mn^{2+} presented a broad-band red emission in the range from 530 to 800 nm, suggesting that there were different luminescence centers. From the normalized PL spectra of LZPO:*x*Mn^{2+} (*x* = 0–0.5) (Fig. 2b), an obvious red-shift of the emission peak from 636 to 672 nm was observed. The emission color under 365 nm wavelength excitation continuously changed from red to deep-red, whereby the corresponding Commission Internationale de l'Eclairage (CIE) color coordinates indicated that red to deep-red phosphors were achieved.

With increasing the doping level, the PL intensity first increased, and then decreased due to the concentration quenching effect (Fig. 2c). The optimal doping concentration was at *x* = 0.2. The internal quantum efficiency (IQE) of the LZPO:0.2Mn^{2+} sample was 53.6% under 416 nm excitation. The emission peak changed from 636 nm at *x* = 0.01 to 672 nm at *x* = 0.3, and then remains unchanged at the higher doping level of *x* = 0.5.

The PL decay curves of LZPO:*x*Mn^{2+} were tested under 412 nm wavelength excitation to further investigate the

luminescence performance. They could be fitted by a second-order exponential function:[45–48]

$$I(t) = A_1 \exp\left(-\frac{t}{\tau_1}\right) + A_2 \exp\left(-\frac{t}{\tau_2}\right) \quad (4)$$

where $I(t)$ is the PL intensity at time t, A_1 and A_2 represent the fitting constants, and τ_1 and τ_2 are the rapid and slow decay times for the exponential components, respectively. The average luminescence lifetime (τ) can be calculated by the following equation:

$$\tau = \frac{A_1\tau_1^2 + A_2\tau_2^2}{A_1\tau_1 + A_2\tau_2} \quad (5)$$

As the Mn^{2+} concentration singly increased, the lifetimes of τ_1, τ_2, and τ for LZPO:$x$$Mn^{2+}$ continuously decreased from 20.29 to 4.76 ms, 41.72 to 18.35 ms, and 40.02 to 16.12 ms, respectively. The lifetimes of τ_1, τ_2, and τ showed the same variation trend, which were caused by the enhanced interaction between the Mn^{2+} ions at a high doping level (Fig. 2d and Table S4, ESI†).

To analyze the luminescence centers of Mn^{2+} ions, the PL spectra of LZPO:$x$$Mn^{2+}$ phosphors were fitted by the Gaussian method and the corresponding lifetimes were measured (Table S5, ESI†). The broad-band red emission of LZPO:$x$$Mn^{2+}$ consisted of two emission peaks (Fig. 3a–c and Fig. S4a–c, ESI†), indicating that the Mn^{2+} ions occupied two different sites. One peak was in the red region (named P1), while the other was in the deep-red region (named P2). The XPS spectrum of the representative LZPO:0.1Mn^{2+} phosphor (Fig. S5, ESI†) revealed photoelectron peaks corresponding to Li 1s, P 2p, O 1s, Zn $2p_{3/2}$, Zn $2p_{1/2}$, and Mn $2p_{3/2}$. The detailed high-resolution XPS spectrum and fitting results of the LZPO:0.1Mn^{2+} phosphor with Mn $2p_{3/2}$ are exhibited in Fig. 3d. The peak at 641.5 eV belonged to the $2p_{3/2}$ of Mn^{2+}, and peak at 643.5 eV belonged to the $2p_{3/2}$ of Mn^{4+}, which further confirmed that the luminescence in this study originated from Mn^{2+} ions.[49] The self-reduction of Mn^{4+} to Mn^{2+} in the air condition was confirmed by the XPS analysis. When Mn^{2+} is doped into the LZPO matrix lattice and sintered in the air condition, it will be oxidized to Mn^{4+} in the beginning. In order to keep the charge balance, one Mn^{4+} will replace two Zn^{2+} sites, leading to the formation of a

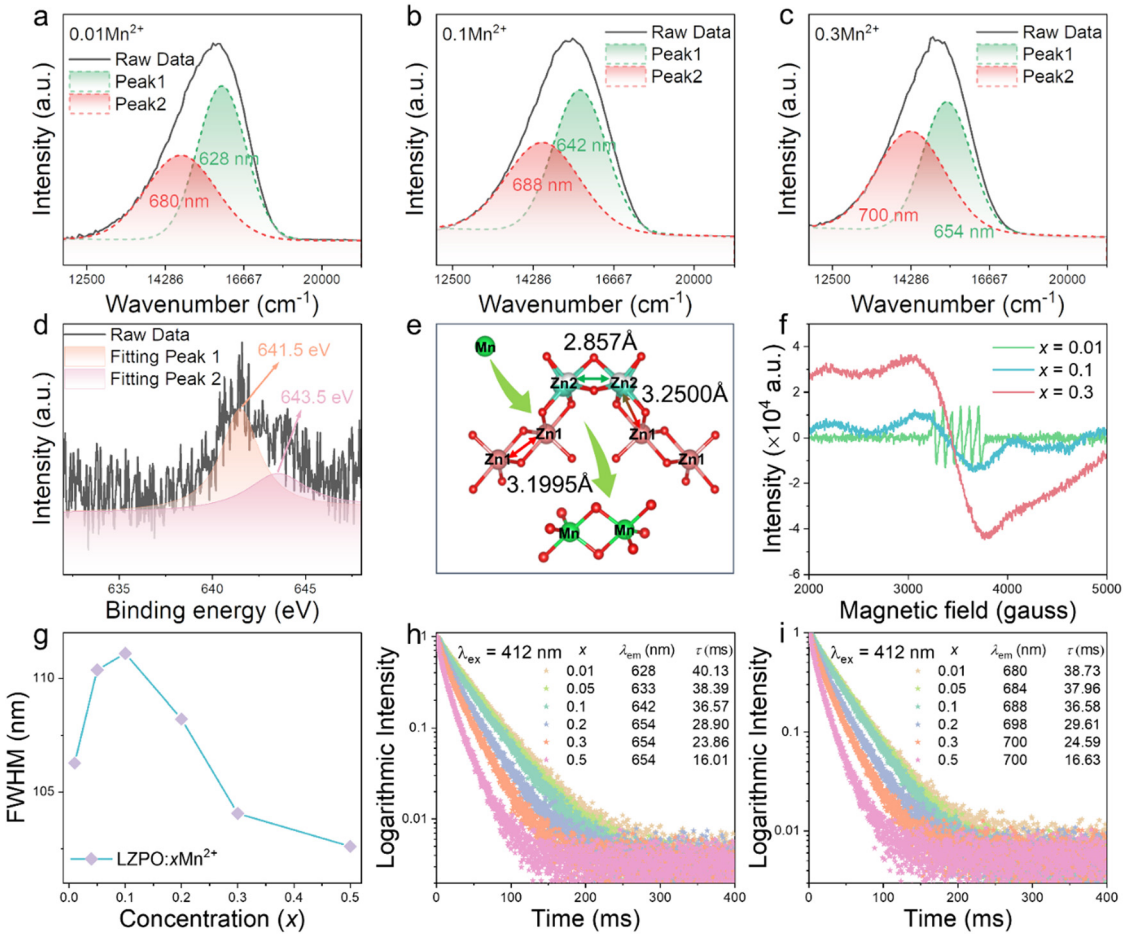

Fig. 3 (a)–(c) Gaussian fitting of LZPO:$x$$Mn^{2+}$ (x = 0.01, 0.1, 0.3). (d) Detailed high-resolution XPS spectrum and fitting results of Mn $2p_{3/2}$ in LZPO:0.1Mn^{2+}. (e) Local structure of [Zn_2O_8] dimers chain. (f) EPR spectra of LZPO:$x$$Mn^{2+}$ (x = 0.01, 0.1, 0.3). (g) Full widths at half maximum (FWHMs) of LZPO:$x$$Mn^{2+}$ (x = 0.01–0.5) samples. (h) and (i) PL decay curves of LZPO:$x$$Mn^{2+}$ (x = 0–0.5) monitored at 628–654 nm and 680–700 nm, respectively, under 412 nm wavelength excitation.

defect with two positive charges. While a vacancy $V_{Zn''}$ is produced with two negative charges at the nearest position. Finally, the two negative charges will be transferred to the Mn^{4+} position to reduce it to Mn^{2+}. As discussed before, Mn^{2+} ions prefer to occupy Zn sites in the lattice. Therefore, P1 in the red region was ascribed to the $^4T_1(^4G) \rightarrow {}^6A_1(^6S)$ transition of the luminescence center of $[MnO_5]$ at Zn sites. From the local structure of the $[Zn_2O_8]$ dimers in Fig. 3e, the distances between Zn1–Zn1, Zn2–Zn2, Zn1–Zn2 were 3.1995 (4), 2.857 (1), and 3.2500 (7) Å, respectively. When the Mn^{2+} ions are doped into the lattice, Mn^{2+} ions will replace Zn^{2+} ions to form Mn–Mn dimers due to the short Zn–Zn distances, which were less than 5 Å.[45] The broad emission P2 should likelyoriginate from the Mn–Mn dimer (named $[Mn_2O_8]$) formed by both Mn^{2+} ions replacing Zn–Zn sites due to the shorter distance.

The luminescence centers of $[MnO_5]$ and $[Mn_2O_8]$ were further verified by the electron paramagnetic resonance (EPR) spectra (Fig. 3f). The well-resolved sextet hyperfine lines were ascribed to the interaction between the electron spin and nuclear spin of isolated Mn^{2+} ions at the low doping level of $x = 0.01$.[50,51] However, the EPR spectra consisted of a singlet structure for $x = 0.1$ and 0.3, and there was less splitting of the sextet hyperfine lines compared to that of the isolated Mn^{2+} ions due to the spin-relaxation processes in the exchange coupling of Mn^{2+} ions.[52,53] This further demonstrated that the red emission in the LZPO:xMn^{2+} system originated from the isolated Mn^{2+} ions and Mn^{2+}–Mn^{2+} dimers. With increasing the Mn^{2+}-doping level, the PL intensity of P2 became stronger, while the PL intensity of P1 decreased. There are two possible reasons to explain this phenomenon. One is the different site-occupation preference at the different doping levels; whereby the Mn^{2+} ions are likely to take up Zn–Zn sites rather than isolated Zn sites at a high doping level due to the shorter distance between Zn^{2+} ions. The other is due to energy transfer from P1 to P2.

The change of full widths at half maximum (FWHMs) as a function of the doping level x is shown in Fig. 3g. At first, the FWHM increased from 106 to 111 nm because of the increase in the PL intensity for P2 emission, reaching its maximum value at $x = 0.1$. Then the FWHM decreased to 103 nm at $x = 0.5$ because of the decrease in PL intensity of the narrower P1 emission at the high-energy site $[MnO_5]$, caused by the energy transfer from $[MnO_5]$ to $[Mn_2O_8]$. In short, the relative PL intensity of these two luminescence centers contribute to the values of the FWHM. This was supported by the analysis of the lifetimes. The lifetime of P1 decreased from 40.13 to 16.01, and 38.73 to 16.63 ms for P2 as the doping level increased (Fig. 3h and i). The apparent difference in lifetime further provided evidence that P1 and P2 came from different luminescence centers. When $x \leq 0.05$, the lifetime of P1 was longer than that of P2; however, the former became lesser than the latter at $x \geq 0.1$, which indicates that there was indeed an energy transfer from P1 to P2.

According to the fitting results, the emissions P1 and P2 were both shifted to longer wavelength with the increase in doping level. P1 was shifted from 628 to 654 nm, and P2 from 680 to 700 nm. To explore the red-shift mechanism of Mn^{2+} emission, three aspects are considered: crystal field, exchange coupling interaction in Mn–Mn dimers, and energy transfer.[54,55] As listed in Table S3 (ESI†), the bond lengths of the nearest neighboring oxygen to Zn were 1.9743, 1.9639, and 1.9142 Å for $x = 0$, 0.01, and 0.2, respectively. With increasing the doping level, the bond length of the nearest neighboring oxygen to Zn tended to decrease. According to the equation:[56]

$$D_q \propto \frac{1}{6R^5} \quad (6)$$

where D_q is the measurement of the crystal field strength, R is the distance between the central ion and its ligands. The increase in Mn^{2+} doping at the smaller Zn^{2+} site leads to a stronger crystal field. As a result, the crystal will be subjected to compression, and then the 3d energy levels of Mn^{2+} ions will be affected by their nearest neighboring oxygen, resulting in a red-shift of Mn^{2+} emission. From the local structure of LZPO, when the Mn^{2+} ions are doped into the lattice, Mn^{2+} ions will replace Zn^{2+} ions to form Mn–Mn dimers due to the short distance between Zn^{2+} ions. The formed Mn–Mn dimers, through exchange coupling interaction in the matrix lattice, will lead to overlapping wavefunctions. The energy difference between the ground state and the first excited state will become smaller, contributing to the emission red-shift. Furthermore, energy transfer between P1 and P2 was verified through the fitted PL spectra and decay curves, which also contribute to the emission red-shift. That is, the emission red-shift was due to a combined effect of the crystal field, exchange coupling interaction in Mn–Mn dimers, and energy transfer.

3.3. PL thermal stability of LZPO:xMn^{2+} phophors

The PL thermal stability is a crucial parameter to ensure the efficient and stable operation of pc-WLED devices at high temperature.[57–60] Temperature-dependent PL spectra of the LZPO:xMn^{2+} phosphors were obtained from 25 °C to 200 °C to evaluate the PL thermal stability. With increasing the ambient temperature, the enhanced thermal motion of molecules strengthened the non-radiative transition, causing a decrease in the PL intensity. Unexpectedly, the PL thermal quenching of the LZPO:0.01Mn^{2+} sample was not obvious in Fig. 4a. The other two high doping levels for the LZPO:0.1Mn^{2+} and LZPO:0.3Mn^{2+} samples were tested to identify if they had excellent PL thermal stability (Fig. 4b and c). Fig. 4d shows a direct-viewing of the emission, including the change in the normalized PL intensity at three doping concentrations with different temperatures. At a low doping level for LZPO:0.01Mn^{2+}, the PL intensity was 97% at 150 °C and 94% at 200 °C of the initial intensity at 25 °C, indicating its superior PL thermostable performance. The PL intensity of LZPO:0.1Mn^{2+} was 94% at 150 °C and 84% at 200 °C of the initial intensity at 25 °C. Even at a higher doping level for LZPO:0.3Mn^{2+}, the PL intensity was 90% at 150 °C and 70% at 200 °C of the initial intensity at 25 °C. The different TQ behaviors with increasing the doping level were caused by the different luminescence centers of $[MnO_5]$ and $[Mn_2O_8]$. As for the luminescence of isolated $[MnO_5]$, only the interactions between the host lattice and activator would influence the PL thermal stability, but

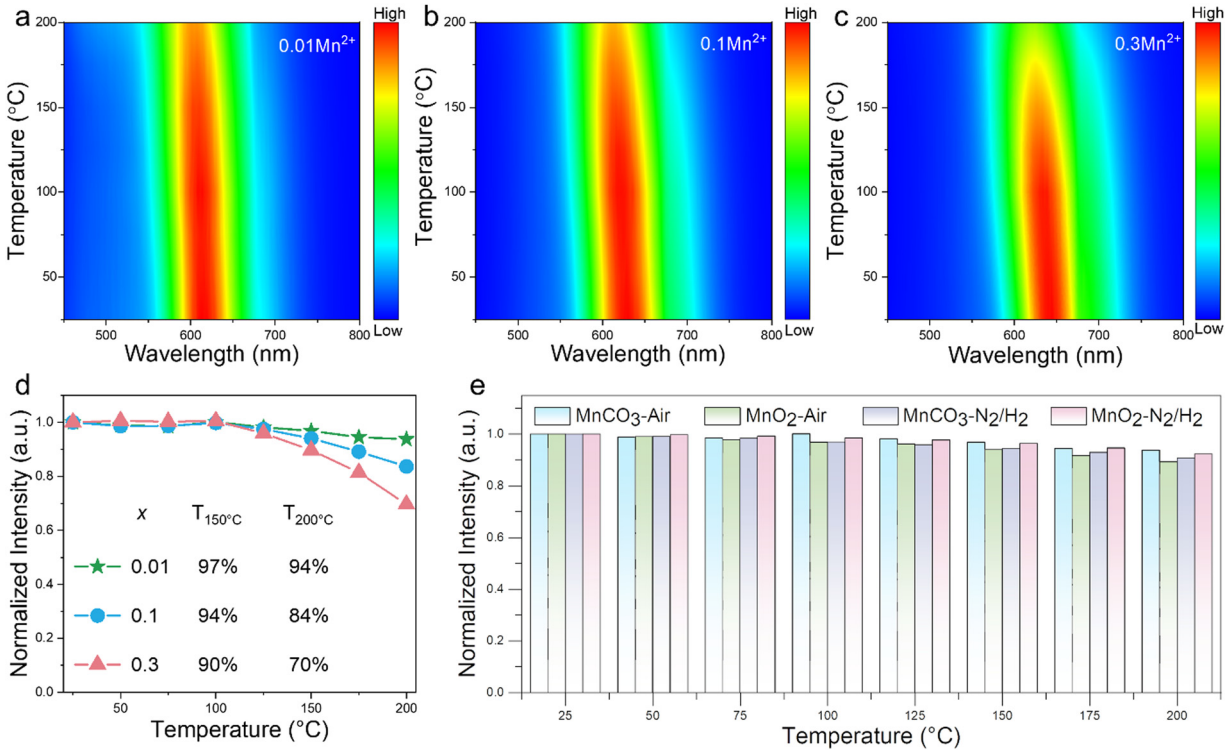

Fig. 4 (a)–(c) Temperature-dependent PL spectra of the LZPO:0.01Mn^{2+}, LZPO:0.1Mn^{2+}, and LZPO:0.3Mn^{2+} samples. (d) Normalized PL intensity of the x = 0.01–0.3 samples under 412 nm excitation as a function of temperature. (e) Normalized PL intensity of LZPO:0.01Mn^{2+} with different Mn sources and sintered conditions.

for the [Mn_2O_8] dimers, the additional interactions between two Mn^{2+} should be considered.[61] The distance between Mn^{2+}–Mn^{2+} will increase at high temperature, reducing the number of [Mn_2O_8] dimers.[62] Consequently, the PL thermal stability of the emission from the isolated Mn^{2+} ions is better than that of the [Mn_2O_8] dimers. The number of [Mn_2O_8] dimer will increase at a higher doping level, resulting in a decrease in the PL thermal stability at high temperature. Furthermore, the temperature-dependent PL spectra of LZPO:0.01Mn^{2+} phosphors with different Mn sources and sintered conditions were measured. As shown in Fig. 4e and Fig. S6 (ESI†), the as-prepared LZPO:0.01Mn^{2+} phosphors exhibited remarkably lower luminescence quenching behaviors, indicating the different Mn sources and sintered conditions had little effect on the PL thermal stability. The above results suggest that the LZPO:Mn^{2+} phosphor is a PL thermally-stable candidate for pc-WLED devices.

To address the lower luminescence quenching behavior, temperature-dependent XRD patterns of LZPO were further measured and are displayed in Fig. 5a. The diffraction peak of the (113) lattice plane shifted from 24.75° at 25 °C to 24.71° at 200 °C. The slight shift of the diffraction peak to the lower angle indicates that the thermal expansion in this lattice was negligible. The corresponding crystallographic parameters and relative values of the volume were almost constant with increasing the temperature (Fig. 5b). The volume expanded by only 0.37% from 1102.22 to 1106.316 Å^3, furtherly identifying the near ZTE performance of LZPO, and indicating the structural stability of LZPO against high temperature. This suggests it provides a stable coordination environment for Mn^{2+} ions, thereby minimizing the emission loss with increasing the temperature. Additionally, thermoluminescence (TL) curves of the LZPO:0.1Mn^{2+} sample were measured to assess the distribution of the trap levels (Fig. 5c). The LZPO:0.1Mn^{2+} phosphor presented two obvious TL glow bands in the range from 303 to 573 K, peaking at 340.2 K and 501.4 K. The corresponding trap depths were estimated to be 0.6804 and 1.0028 eV according to the Urbach formula: $E_T = E_m/500$.[51] Moreover, the intensity of trap A was much stronger than that of trap B, indicating that most trap levels were located in the shallow region in the forbidden band. Thereby the traps-assisted energy transfer to the luminescent center would compensate for the luminous loss due to the non-radiative transition. A schematic diagram of the mechanism of the luminescence process is shown in Fig. 5d. In this mechanism, under 412 nm wavelength excitation, electrons at the $^6A_1(^6S)$ (for [MnO_5]) or $^6A_1(^6S)$ $^6A_1(^6S)$ (for [Mn_2O_8] dimer) ground state are promoted to the excited level [$^4A_1(^4G)$,$^4E(^4G)$], then move to the first excited state $^4T_1(^4G)$ (for [MnO_5]) or $^6A_1(^6S)^4T_1(^4G)$ (for [Mn_2O_8] dimer) through a non-radiative relaxation process. Then the excited electrons come back to the ground state to generate red and deep-red emission. There is an energy transfer from [MnO_5] to the [Mn_2O_8] dimer. Besides, some excited electrons will be captured by traps formed in the process of self-reduction. Stimulated by thermal activation, these will be released back into conduction band (CB) and will arrive at the first excited state $^4T_1(^4G)$ or $^6A_1(^6S)^4T_1(^4G)$ through a non-radiative relaxation process to participate in the radiation transition. As a

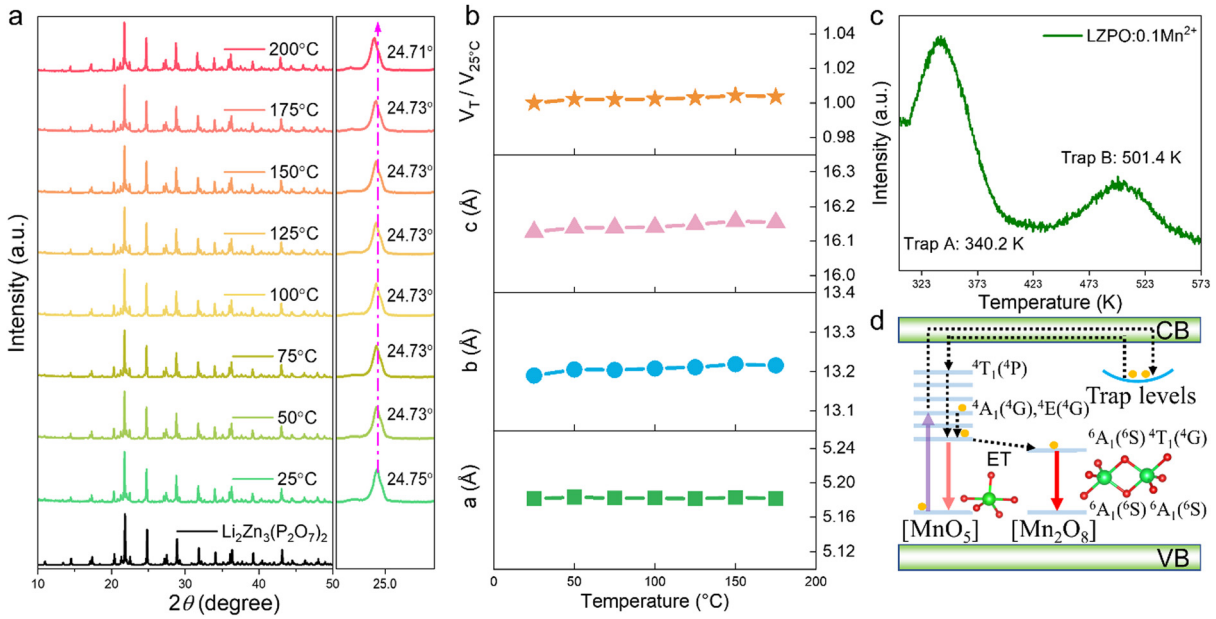

Fig. 5 (a) XRD patterns of the LZPO host from 25 °C to 200 °C. (b) Cell parameters (a)–(c) and volume ration of $V_T/V_{25\,°C}$ as a function of temperature. (c) TL spectrum of the LZPO:0.1Mn^{2+} sample. (d) Luminescence mechanism diagram for the LZPO:xMn^{2+} phosphor.

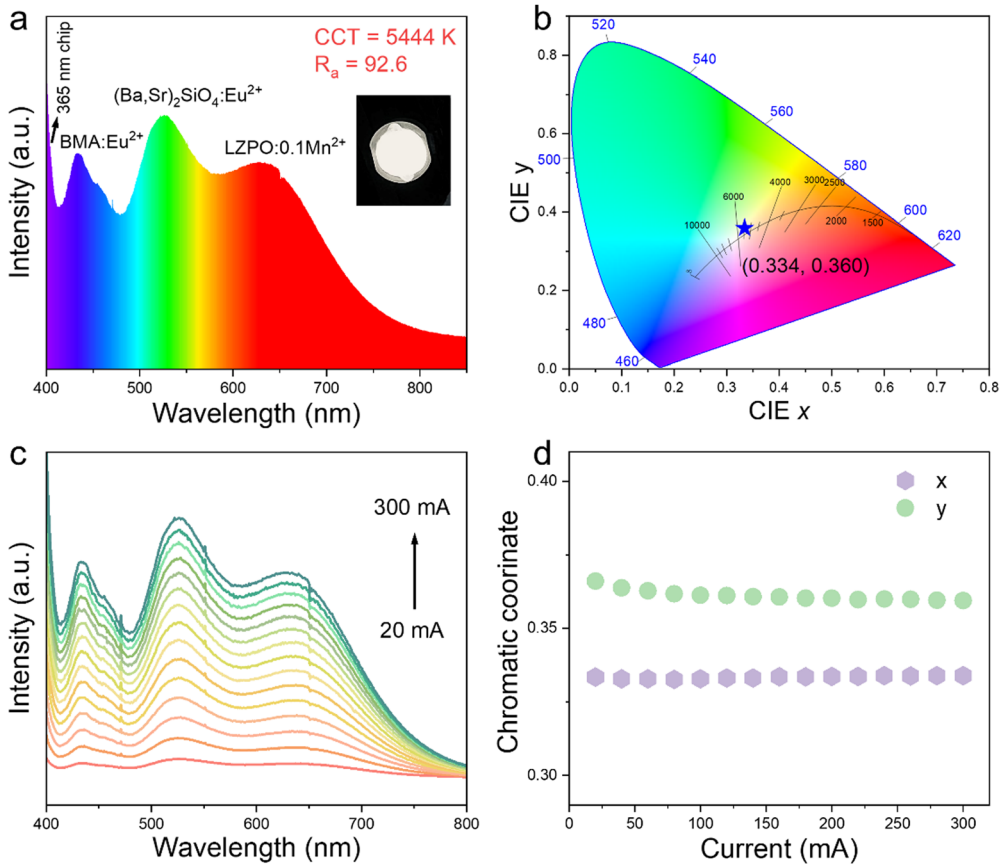

Fig. 6 (a) Electroluminescence spectrum of the pc-WLED device fabricated with an n-UV LED chip (λ_{ex} = 365 nm), commercial blue BAM:Eu^{2+}, green $(Ba,Sr)_2SiO_4$:Eu^{2+}, and as-prepared red LZPO:0.1Mn^{2+} phosphors. (b) CIE chromaticity coordinates of the as-fabricated pc-WLED. (c) EL spectra of the fabricated pc-WLED device at currents of 20–300 mA. (d) Change in the chromatic coordinates (*x*, *y*) with increasing the current from 20 to 300 mA.

result, the emission loss is compensated by the process of the traps-assisted energy transfer. The stable coordination environment and traps-assisted energy transfer demonstrate that the LZPO:Mn^{2+} phosphor is a superior thermostable luminescent material, making it a hopeful candidate for high-power lighting equipment.

3.4. Potential pc-WLED applications

A pc-WLED device was fabricated by mixing a moderate amount of commercial blue phosphor [$BaMgAl_{11}O_{17}$:Eu^{2+} (BAM:Eu^{2+})], green phosphor [$(Ba,Sr)_2SiO_4$:Eu^{2+}], and the as-prepared LZPO:0.1Mn^{2+} phosphor with a commercial 365 nm UV chip. As shown in Fig. 6a and b, the warm pc-WLED presented a low correlated color temperature (CCT) = 5444 K, and high color rendering index (CRI) of 92.6, with the CIE color coordinate of (0.334, 0.360) under a voltage of 3.3 V and current of 300 mA. The luminous efficiency of the pc-WLED was 1.7 Im W^{-1} under 3.2 V and 60 mA. These values of the pc-WLED are relatively low, and so it would be meaningful to develop new Mn-doped materials with high luminous efficiency in the future. The emission intensity of the as-prepared pc-WLED device gradually increased with increasing the current from 20–300 mA (Fig. 6c). In addition, changes in CIE coordinates for the pc-WLED device were not obvious at different currents (Fig. 6d), indicating the excellent color stability of the fabricated pc-WLED device.

4. Conclusion

In summary, a series of red-emitting LZPO:*x*Mn^{2+} phosphors were successfully synthesized by a high-temperature solid-state reaction process in an ambient atmosphere. Two luminescence centers [MnO_5] and [Mn_2O_8] were identified, which resulted in a broad red emission. Under 412 nm wavelength excitation, the emission peak showed a red-shift from 636 to 672 nm with increasing the doping levels of Mn^{2+} due to a combined effect of the strengthened crystal field, exchange coupling interaction in Mn–Mn dimers, and energy transfer. Interestingly, the LZPO:*x*Mn^{2+} phosphors exhibited excellent PL thermal stability. The PL intensity was 97% for LZPO:0.01Mn^{2+} and 90% for the heavily doped LZPO:0.3Mn^{2+} at 150 °C compared with their initial intensity at 25 °C, indicating their superior PL thermostable performance. The superior PL thermal stability supported by the structural stability of the near-zero thermal expansion (NZTE) LZPO against high temperature was also certified. Eventually, a pc-WLED device was fabricated to highlight the great application potential (CCT = 5444 K, Ra = 92.6). In light of the above results, the excellent PL thermostable LZPO:Mn^{2+} phosphor is considered a potential candidate for applications in pc-WLED devices. This study not only provides comprehensive evidence to discuss the relationship between the optical properties and crystal structure, but enriches the choices to develop novel functional optical materials by taking advantage of near-zero thermal expansion matrices.

Author contributions

All authors have given approval to the final version of the manuscript.

Conflicts of interest

There are no conflicts to declare.

Acknowledgements

This work was financially supported by the National Science and Technology Major Project (2022YFB3503800), the Projects for Science and Technology Development Plan of Jilin Province (20210402046GH), the National Natural Science Foundation of China (NSFC No. 51932009, 51929201, 52072349, 52172166), the Natural Science Foundation of Zhejiang Province (LR22E020004), the Project funded by China Postdoctoral Science Foundation (2022TQ0365). M. S. Molokeev and S. P. Polyutov acknowledge the support by the Ministry of Science and High Education of Russian Federation (Project No. FSRZ-2023-0006).

Notes and references

1 Y. H. Kim, P. Arunkumar, B. Y. Kim, S. Unithrattil, E. Kim, S.-H. Moon, J. Y. Hyun, K. H. Kim, D. Lee, J.-S. Lee and W. B. Im, *Nat. Mater.*, 2017, **16**, 543–550.
2 Y. Wang, J. Ding, Y. Li, X. Ding and Y. Wang, *Chem. Eng. J.*, 2017, **315**, 382–391.
3 G. B. Nair, H. C. Swart and S. J. Dhoble, *Prog. Mater. Sci.*, 2020, **109**, 100622.
4 X. Zhou, J. Qiao and Z. Xia, *Chem. Mater.*, 2021, **33**, 1083–1098.
5 M.-H. Fang, Z. Bao, W.-T. Huang and R.-S. Liu, *Chem. Rev.*, 2022, **122**, 11474–11513.
6 N. M. C. H. P. Lan, P. Van Huan, N. H. Thong, D.-H. Nguyen, N. D. T. Kien, C. M. Nhuong, C. X. Thang and V.-H. Pham, *Luminescence*, 2022, **37**, 577–587.
7 S. Huang, M. Shang, Y. Yan, Y. Wang, P. Dang and J. Lin, *Laser Photonics Rev.*, 2022, **16**, 2200473.
8 M. Zhao, Q. Zhang and Z. Xia, *Mater. Today*, 2020, **40**, 246–265.
9 M. Wang, X. Ming, J. Cao, L. Yang, Z. Wang, C. Ma, M. Zhang and W. Liu, *Inorg. Chem.*, 2023, **62**, 75–86.
10 M. Zhao, H. Liao, M. S. Molokeev, Y. Zhou, Q. Zhang, Q. Liu and Z. Xia, *Light Sci. Appl.*, 2019, **8**, 1–9.
11 P. Dang, W. Wang, H. Lian, G. Li and J. Lin, *Adv. Opt. Mater.*, 2022, **10**, 2102287.
12 Y. Wei, H. Yang, Z. Gao, X. Yun, G. Xing, C. Zhou and G. Li, *Laser Photonics Rev.*, 2021, **15**, 2000048.
13 Y. Wang, J. Ding, Y. Wang, X. Zhou, Y. Cao, B. Ma, J. Li, X. Wang, T. Seto and Z. Zhao, *J. Mater. Chem. C*, 2019, **7**, 1792–1820.
14 R. Bajaj, P. Rohilla, A. Prasad, Ravita, A. Shandilya and A. S. Rao, *Luminescence*, 2023, **38**, 428–436.
15 Y. Bai, S. Sun, L. Wu, T. Hu, L. Zheng, L. Wu, Y. Kong, Y. Zhang and J. Xu, *J. Mater. Chem. C*, 2022, **10**, 4317–4326.
16 H. Chen, Y. Lei, J. Li, K. Chen, L. Wu, L. Zheng, T. Sun, Y. Kong, Y. Zhang and J. Xu, *Inorg. Chem.*, 2022, **61**, 5495–5501.
17 S. Li, W. Hu, M. G. Brik, S. Lian and Z. Qiu, *Inorg. Chem. Front.*, 2022, **9**, 3224–3232.

18 L. Wu, S. Sun, Y. Bai, Z. Xia, L. Wu, H. Chen, L. Zheng, H. Yi, T. Sun, Y. Kong, Y. Zhang and J. Xu, *Adv. Opt. Mater.*, 2021, **9**, 2100870.
19 Z. Long, Y. Wen, J. Qiu, J. Wang, D. Zhou, C. Zhu, J. Lai, X. Xu, X. Yu and Q. Wang, *Chem. Eng. J.*, 2019, **375**, 122016.
20 R. Shi, L. Ning, Z. Wang, J. Chen, T. Sham, Y. Huang, Z. Qi, C. Li, Q. Tang and H. Liang, *Adv. Opt. Mater.*, 2019, **7**, 1901187.
21 Y. Wei, H. Yang, Z. Gao, Y. Liu, G. Xing, P. Dang, A. A. A. Kheraif, G. Li, J. Lin and R.-S. Liu, *Adv. Sci.*, 2020, **7**, 1903060.
22 S. He, L. Zhang, H. Wu, H. Wu, G. Pan, Z. Hao, X. Zhang, L. Zhang, H. Zhang and J. Zhang, *Adv. Opt. Mater.*, 2020, **8**, 1901684.
23 Q. Dong, J. Cui, Y. Tian, J. Jia, F. Yang, F. Du, J. Peng, X. Ye and S. Yang, *CrystEngComm*, 2019, **21**, 5947–5957.
24 Y.-T. Tsai, C.-Y. Chiang, W. Zhou, J.-F. Lee, H.-S. Sheu and R.-S. Liu, *J. Am. Chem. Soc.*, 2015, **137**, 8936–8939.
25 D. Wen, H. Liu, Y. Guo, Q. Zeng, M. Wu and R. S. Liu, *Angew. Chem., Int. Ed.*, 2022, **61**, e202204411.
26 W. Wang, H. Yang, M. Fu, X. Zhang, M. Guan, Y. Wei, C. C. Lin and G. Li, *Chem. Eng. J.*, 2021, **415**, 128979.
27 W. Wang, M. Fu, S. Liu, X. Zhang, Y. Wei and G. Li, *J. Lumin.*, 2022, **242**, 118536.
28 P. Dang, G. Li, X. Yun, Q. Zhang, D. Liu, H. Lian, M. Shang and J. Lin, *Light: Sci. Appl.*, 2021, **10**, 29.
29 J. Liao, M. Wang, F. Lin, Z. Han, B. Fu, D. Tu, X. Chen, B. Qiu and H.-R. Wen, *Nat. Commun.*, 2022, **13**, 2090.
30 J. Zhang, G.-M. Cai, L.-W. Yang, Z.-Y. Ma and Z.-P. Jin, *Inorg. Chem.*, 2017, **56**, 12902–12913.
31 Y. Liu, G. Zhang, J. Huang, X. Tao, G. Li and G. Cai, *Inorg. Chem.*, 2021, **60**, 2279–2293.
32 L. Ji, H. Ma and J. Liang, *Acta Crystallogr. C*, 2009, **65**, 30–32.
33 S. Wu, S. Hu, Q. Liu, S. Zhang, D. Jiang, G. Zhang, Y. Le, Y. Xiao, B. Xiao, P. Xiong, Y. Chen and Y. Wang, *J. Mater. Chem. C*, 2023, **11**, 3865–3874.
34 L. Wu, Y. Bai, L. Wu, H. Yi, X. Zhang, L. Zhang, Y. Kong, Y. Zhang and J. Xu, *Dalton Trans.*, 2018, **47**, 13094–13105.
35 Y. Wang, Y. Zhou, H. Ming, Y. Zhao, E. Song and Q. Zhang, *ACS Appl. Mater. Interfaces*, 2021, **13**, 51255–51265.
36 Y. Meng, P. Chen, H. Fan, Z. Lu, X. Zhong, J. Lu, Y. Ou and L. Zhou, *Mater. Res. Bull.*, 2022, **147**, 111610.
37 M. D. Dramićanin, L. Marciniak, S. Kuzman, W. Piotrowski, Z. Ristić, J. Periša, I. Evans, J. Mitrić, V. Đorđević, N. Romčević, M. G. Brik and C.-G. Ma, *Light Sci. Appl.*, 2022, **11**, 279.
38 Z. Liao, H. Xu, W. Zhao, H. Yang, J. Zhong, H. Zhang, Z. Nie and Z.-K. Zhou, *Chem. Eng. J.*, 2020, **395**, 125060.
39 Z. Ristić, W. Piotrowski, M. Medić, J. Periša, Ž. M. Antić, L. Marciniak and M. D. Dramićanin, *ACS Appl. Electron. Mater.*, 2022, **4**, 1057–1062.
40 Y. Zhu, Y. Liang, S. Liu, H. Li and J. Chen, *Adv. Opt. Mater.*, 2019, **7**, 1801419.
41 Y. Wei, G. Xing, K. Liu, G. Li, P. Dang, S. Liang, M. Liu, Z. Cheng, D. Jin and J. Lin, *Light: Sci. Appl.*, 2019, **8**, 15.
42 A. J. van Bunningen, A. D. Sontakke, R. van der Vliet, V. G. Spit and A. Meijerink, *Adv. Opt. Mater.*, 2023, **11**, 2202794.
43 E. H. Song, Y. Y. Zhou, Y. Wei, X. X. Han, Z. R. Tao, R. L. Qiu, Z. G. Xia and Q. Y. Zhang, *J. Mater. Chem. C*, 2019, **7**, 8192–8198.
44 S.-Y. Zhu, D. Zhao, S.-J. Dai, R.-J. Zhang and L.-Y. Shi, *CrystEngComm*, 2022, **24**, 2966–2975.
45 E. Song, X. Jiang, Y. Zhou, Z. Lin, S. Ye, Z. Xia and Q. Zhang, *Adv. Opt. Mater.*, 2019, **7**, 1901105.
46 Z. Yang, Y. Zhao, Y. Zhou, J. Qiao, Y.-C. Chuang, M. S. Molokeev and Z. Xia, *Adv. Funct. Mater.*, 2022, **32**, 2103927.
47 G. Liu, T. Hu, M. S. Molokeev and Z. Xia, *iScience*, 2021, **24**, 102250.
48 C. Yang, C. Fan, F. Hussain, W. Sheng, K. Song, J. Wu, Q. Huang, W. Su, J. Xu, S. Sun and D. Wang, *J. Rare Earths*, 2023, **41**, 489–497.
49 Y. Chen, J. Chen, J. Liang, J. He, Z.-Q. Liu and Y. Yin, *Chem. Mater.*, 2020, **32**, 9551–9559.
50 J. Xue, T. Hu, F. Li, F. Liu, H. M. Noh, B. R. Lee, B. C. Choi, S. H. Park, J. H. Jeong and P. Du, *Laser Photonics Rev.*, 2023, **17**, 2200832.
51 Z.-H. Zuo, Y.-Y. Peng, J. Li, X. Wang, Z.-Q. Liu and Y. Chen, *Chem. Eng. J.*, 2022, **446**, 136976.
52 E. Song, J. Wang, S. Ye, X.-B. Yang, M. Peng, Q. Zhang and L. Wondraczek, *Adv. Opt. Mater.*, 2017, **5**, 1700070.
53 X. Li, T. Liu, K. Zhang, Z. Hu, H. An, S. Deng, Y. Kong and B. Wang, *J. Mater. Chem. C*, 2023, **11**, 712–721.
54 L. Shi, Y. Huang and H. J. Seo, *J. Phys. Chem. A*, 2010, **114**, 6927–6934.
55 D. Wei and H. J. Seo, *J. Lumin.*, 2021, **229**, 117644.
56 W. Wang, H. Yang, Y. Liu, X. Yun, Y. Wei and G. Li, *CrystEngComm*, 2020, **22**, 311–319.
57 L. Zhou, W. Wang, D. Xu, Z. Wang, Z. Yi, M. Wang and Z. Lu, *Ceram. Int.*, 2021, **47**, 34820–34827.
58 Y. Wei, H. Yang, Z. Gao, Y. Liu, G. Xing, P. Dang, A. A. A. Kheraif, G. Li, J. Lin and R. Liu, *Adv. Sci.*, 2020, **7**, 1903060.
59 Z. Xia, X. Wang, Y. Wang, L. Liao and X. Jing, *Inorg. Chem.*, 2011, **50**, 10134–10142.
60 Z. Wang, S. Liang, C. Zhan, K. Xu, J. Hu, D. Chen, L. Song and H. Zhu, *J. Rare Earths*, DOI: **10.1016/j.jre.2023.04.014**.
61 E. Song, M. Chen, Z. Chen, Y. Zhou, W. Zhou, H.-T. Sun, X. Yang, J. Gan, S. Ye and Q. Zhang, *Nat. Commun.*, 2022, **13**, 1–9.
62 E. Song, S. Ye, T. Liu, P. Du, R. Si, X. Jing, S. Ding, M. Peng, Q. Zhang and L. Wondraczek, *Adv. Sci.*, 2015, **2**, 1500089.